Supplementary Information (SI) for Materials Horizons.
This journal is © The Royal Society of Chemistry 2024

Supplementary Information for

Synaptic memristors based on BTO thin-film irradiated by swift heavy ions for neuromorphic computing

Minghui Xu,‡[a] Tao Liu,‡*[a] Hailian Li,[a] Yong Liu,*[b] Pengshun Shan,[b] Ruowei Wang,[b] Weijin Kong,*[a] Minghao Zhang,[b] Shuangqing Fan,[a] and Jie Su *[a, c]

a. College of Electronic and Information Engineering, College of Physics Science, Qingdao University, Qingdao 266071, China. E-mail: liutao@qdu.edu.cn, E-mail: kwjsd@163.com, E-mail: jsu@qdu.edu.cn
b. School of Energy and Power Engineering, Shandong University, Jinan 250061, China. E-mail: yongliu@sdu.edu.cn
c. National Laboratory of Solid State Microstructures, Physics Department, Nanjing University, Nanjing 210093, China

‡ These authors equally contributed to this work.

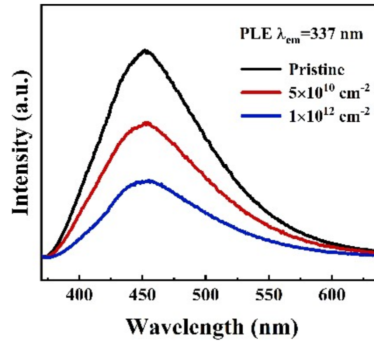

Fig. S1 PL spectra for the BaTiO3 samples via Xe31+ irradiation with different fluences.

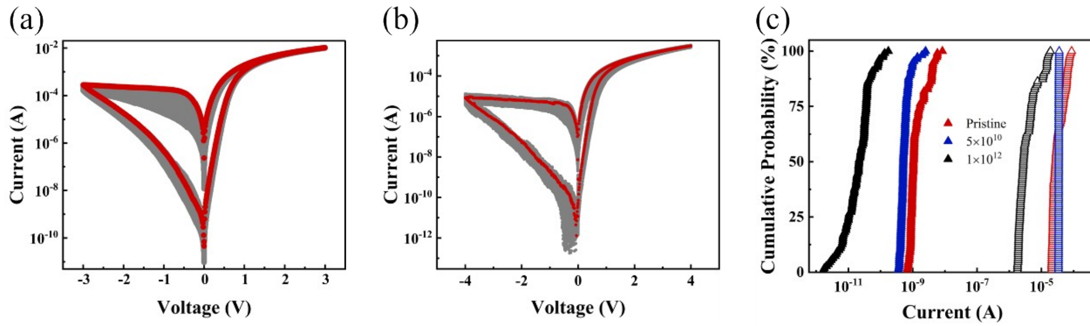

Fig. S2 I-V characteristics. I-V curves after 100 DC voltage scans for (a) D0 and (b) D2. (c) Cumulative probability distributions of HRS and LRS forD0, D1, and D2.

To measure the inter-device variation of the set voltage, we measured the I-V curves of 100 sets of Pt/BTO/NSTO devices[1, 2]. The set resistance is defined as the resistance when the voltage level reached 0.3 V during the setup process. The device-to-device variation of the set resistance is quantitatively evaluated by σ/μ, which is the ratio of the standard deviation (σ) to the mean (μ) of the set resistance[3]. The inter-week fluctuations (standard deviation (σ)/mean (μ)) of the LRS and HRS of D0 are as high as 47% and 82%, respectively. Additionally, the inter-week fluctuations of the LRS and HRS of D2 device are as high as 78% and 97%, respectively.

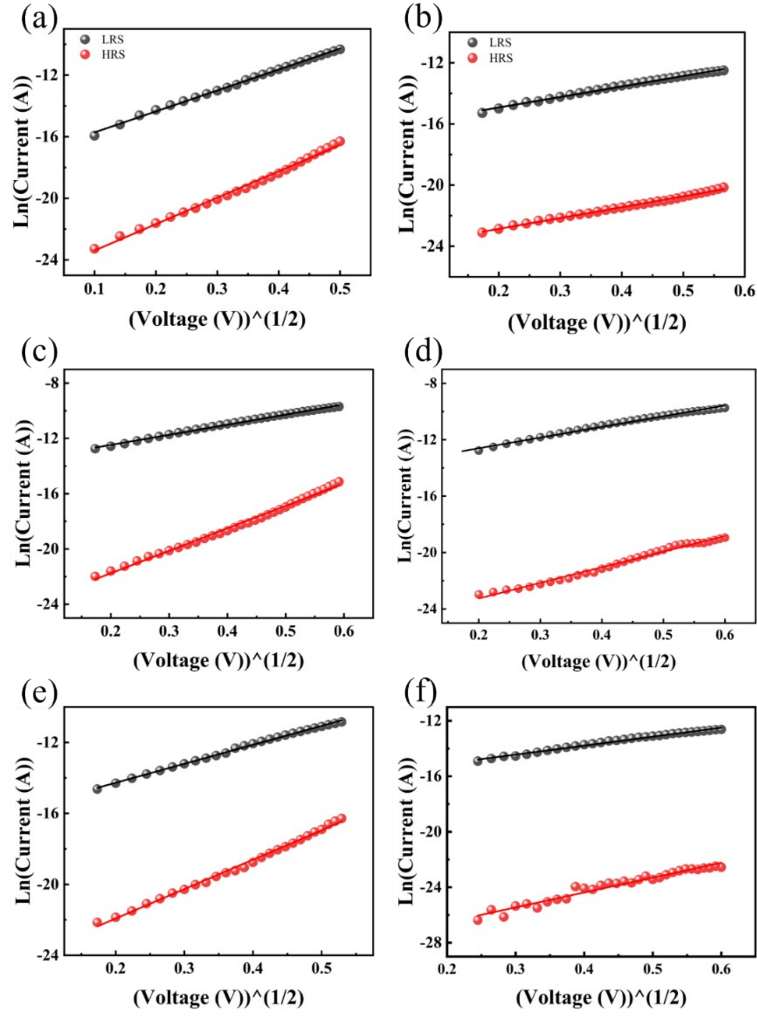

Fig. S3 Resistive mechanism of Pt/BTO/NSTO memristors: partial *I-V* curve fits for the D0 at (a) positive and (b) negative voltages, the D1 at (c) positive and (d) negative voltages, and the D2 at (e) positive and (f) negative voltages.

The structure of the device is a metal-oxide ferroelectric-semiconductor structure, and previous studies in the literature related to similar structures have shown that this structure usually generates a Schottky barrier at the interface between the oxide ferroelectric and the semiconductor, and the conductive mechanism is usually a Schottky-emission conductive mechanism, and the formula for Schottky emission is:[4]

$$I = AT^2 Sexp\left[-\frac{\varphi - \sqrt{\frac{q^3 V}{4\pi\varepsilon d}}}{k_B T}\right] \#(1)$$

where A is the effective Richardson constant, T is the temperature, S is the device junction area, q is the electron charge, φ is the barrier size, k_B is the Boltzmann constant, ε is the dielectric constant, and d is the film thickness. In order to determine the compliance, we selected the *I-V* characteristic curves of the device in the region of 0 V~0.25 V, 0 V~-0.25 V where the barriers of the high and low resistance states are basically stable, and carried out the fitting of the Schottky emission formula, as shown in Fig. S3, and it can be seen that the fitting results are very perfect.

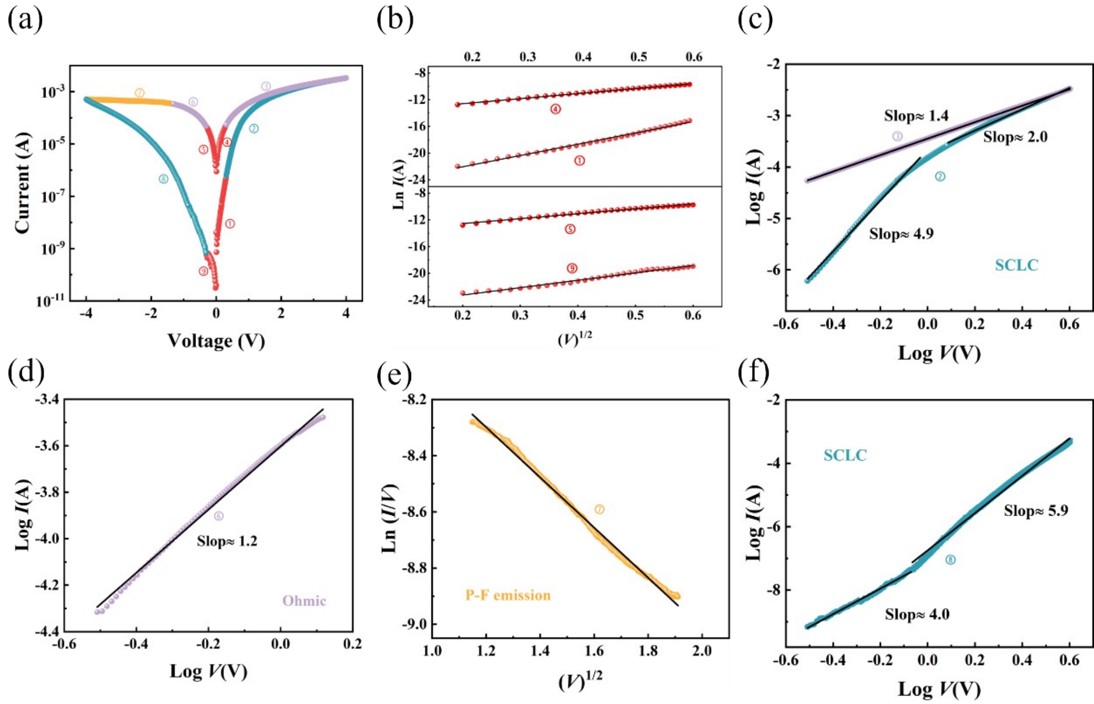

Fig. S4 Plots of the *I–V* curves in (a) shown on different scales to reveal the conduction mechanisms: (b) ln(*I*/*V*) vs (*V*) $^{1/2}$ in the positive and negative bias region; (c) SCLC under positive bias; (d) Omhic in the negative bias region;(e) ln(*I*/*V*) vs (*V*) $^{1/2}$ in the negative bias region; (f) SCLC in the negative bias region.

To gain deeper insights into the physical mechanisms of the memristor with 5×10^{10} fluence, the *I-V* curve was divided into nine processes to be fitted, as shown in Fig S4a. According to the results, the main mechanisms of the device were Schottky, Space Charge Limited Current (SCLC), Omhic and Pool–Frenkel (P–F) emission conduction.[5-7] In Fig. S4(b), the curve illustrates the low voltage region of the *I-V* characteristic curve associated with the Schottky contact mechanism. As shown in Fig. S4(c) and S4(f), the *I-V* curves are linear in Processes 2 and 8, indicating that the RS at this point conforms to the Space Charge Limited Current (SCLC) mechanism, the formula as follows:

$$I = \frac{9}{8}\mu\varepsilon\frac{V^2}{d^3}S\#(2)$$

where μ is the electron mobility, ε is the dielectric constant, V is the applied voltage, d is the film thickness, and S is the device junction area. At this point, the curve satisfies the linear relationship in log I -log V coordinates and the slope is 2. As the voltage continues to increase, the *I-V* curve still adheres to Eq. 1. However, the difference compared to the previous stage is that the linear slope changes to n (n ≥ 3). This implies that conductive transport is significantly influenced by membrane defects like oxygen vacancies. The curve of ln(*I*/*V*) vs (*V*) $^{1/2}$ negative bias region (process 7) is shown in Fig. S4(e), where the linear behavior corresponds to the Poole-Frenkel (P-F) emission mechanism. The P-F emission mechanism's equation is as follows:

$$I = q\mu N_c SV exp\left[-\frac{q\varphi - \sqrt{\frac{q^3V}{\pi\varepsilon}}}{k_BT}\right]\#(3)$$

where q is the electron charge, μ is the electron mobility, N_c is the density of conduction band states, S is the device junction area, $q\varphi$ is the trap energy level, k_B is the Boltzmann constant, ε is the dielectric constant, and T is the temperature. In the Poole-Frenkel (P-F) emission mechanism, the *I-V* curve demonstrates a linear correlation in the coordinates ln (I/V) ~ (V) $^{1/2}$. The slopes of the fitted *I-V* curves for processes 3 and

6 are 1.4 and 1.2, respectively, indicating ohmic conduction in the LRS and the formation of conductive filaments in the process. We have added the explanations in the Supplement Information.

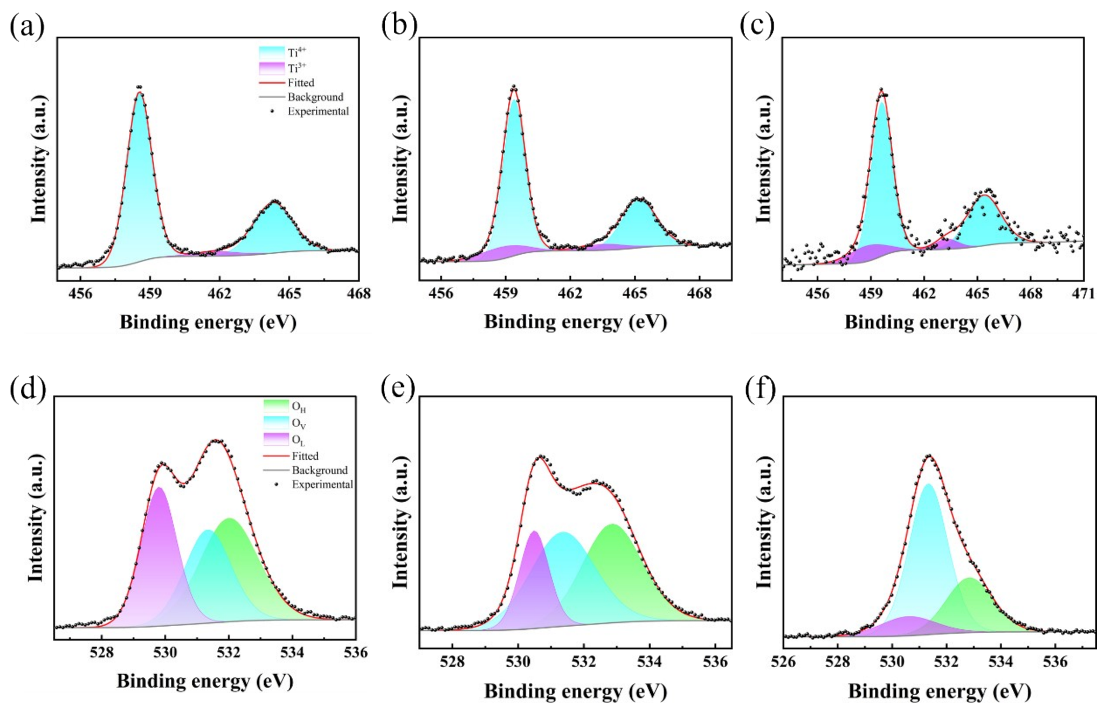

Fig. S5 (a), (d) XPS spectra of Ti 2*p* and O1*s* of D0. (b), (e) XPS spectra of Ti 2*p* and O 1*s* of D1. (c), (f) XPS spectra of Ti 2*p* and O 1*s* of D2.

The peaks at 532.8, 531.9, and 530.6 eV correspond to adsorbed oxygen (O_H), vacancy oxygen (O_V), and lattice oxygen (O_L), respectively. The O_V concentrations are 0.154, 0.406, and 0.673, and the Ti^{3+}/Ti^{4+} ratios are 0.005, 0.097, and 0.203, respectively, which become larger with the increase of irradiation fluence.

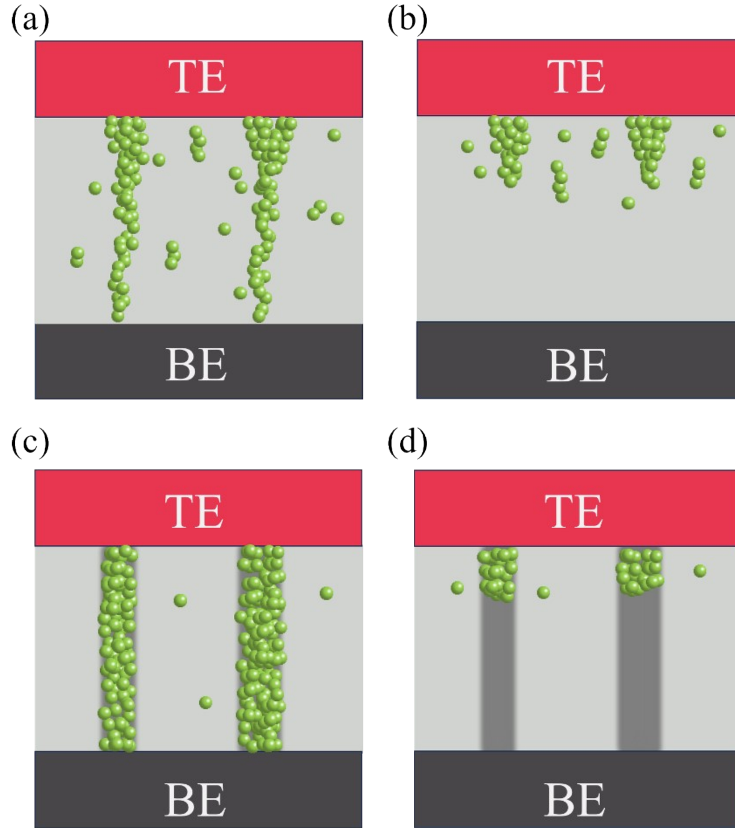

Fig. S6 Schematic illustrations of the different RS mechanisms of Pt/BTO/NSTO memristors: for the D0 at (a) LRS and (b) HRS; the D1 at (c) LRS and (d) HRS.

To better explain the mechanism, we give Fig. S6. As can be seen in Fig. S6(c), ion track damage occurs within the BTO films of D1. In the low resistance states (LRS), the conductive filaments formed is thicker than the conductive filaments of D0 (Fig. S6(a)). Therefore, the LRS is lower than that of D0. In addition, we can find that at the high resistance states (HRS), there are more oxygen vacancies left in the film of D0 (Fig. S6(b)). Therefore, its HRS is lower than that of D1. These are why ion irradiation increases the ON/OFF ratio.

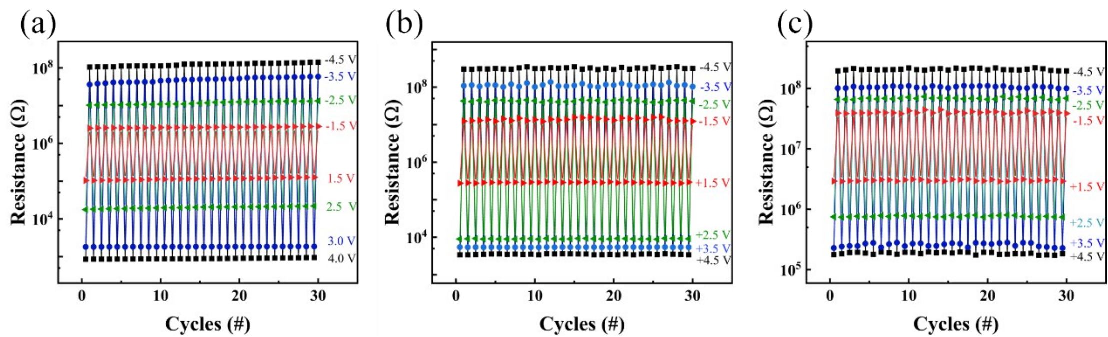

Fig. S7 Resistance switching among different resistance states by applying different voltage for (a) D0, (b) D1, and (c) D2.

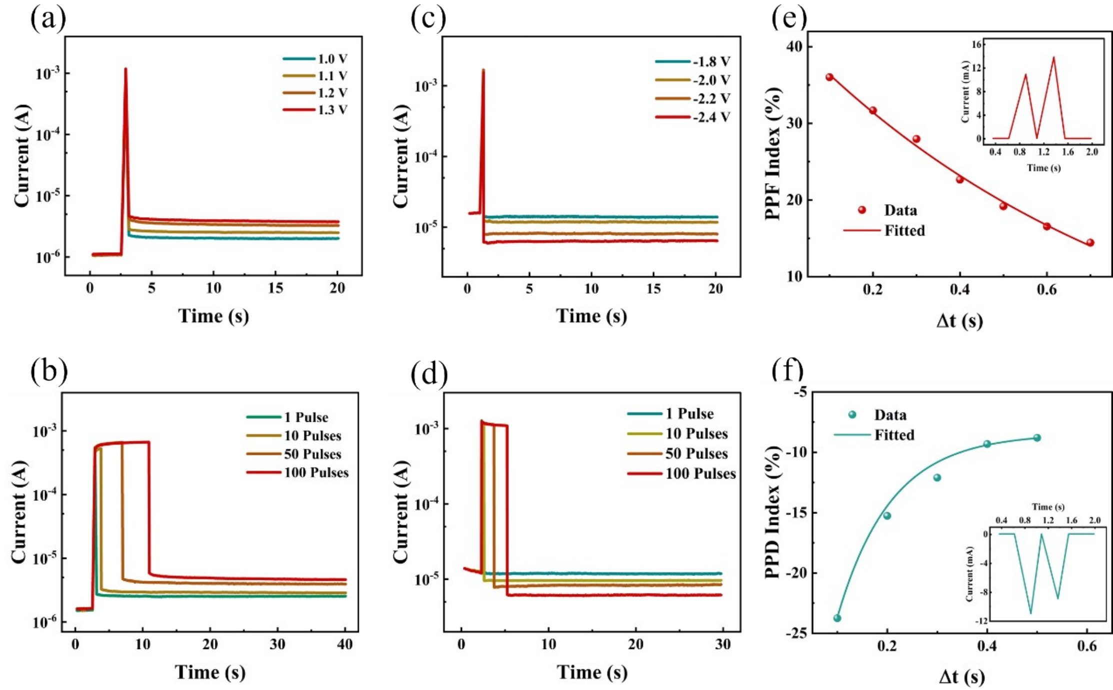

Fig. S8 (a) EPSC with different pulse amplitudes and b) different number of pulses. (c) IPSC with different pulse amplitudes and (d) different number of pulses. (e) PPF and (f) PPD (insets show the PPF/PPD behavior of the pulse-excited devices).

Simulations of the synaptic plasticity function for devices irradiated with 1×10^{12} cm^{-2} are shown in Fig. S8. These results show that the change in device conductance depends on the pulse amplitude and the time interval of the applied pulses, demonstrating a great potential in modelling the long-term and short-term plasticity of synapses.

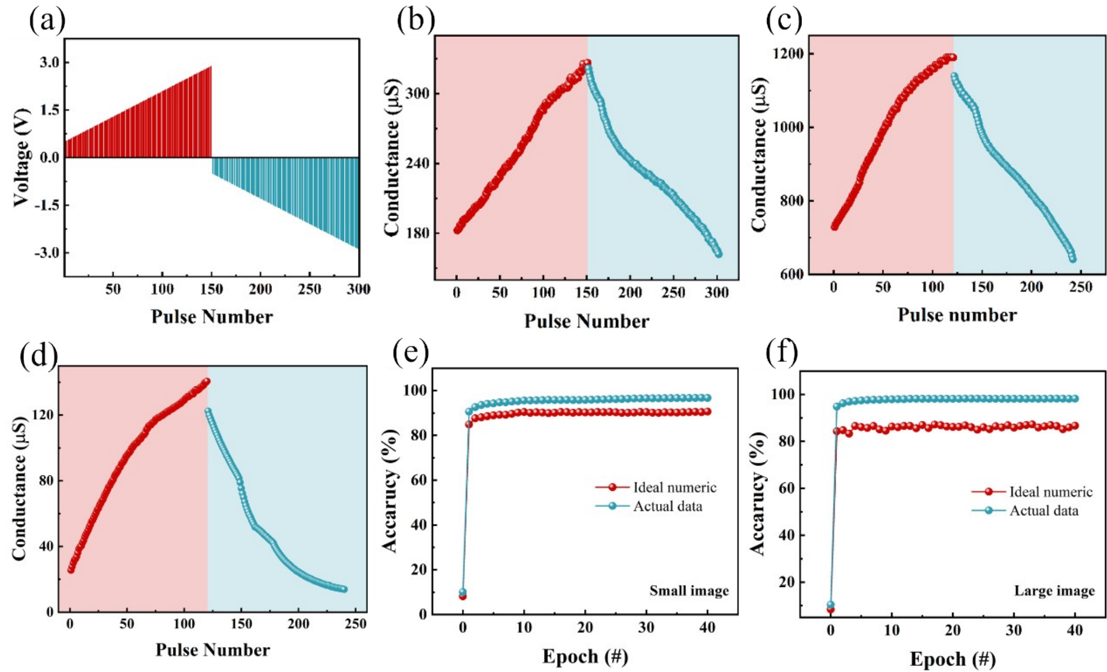

Fig. S9 (a) Programming scheme simulating the process of successive synaptic enhancement and depression. (b), (c) and (d) indicate LTP and LTD for D1, D2 and D0, respectively. D0 of training accuracies for (e) the small image test dataset and (f) the large image test dataset.

Fig. S9 shows the conductance modulation of synapses, including LTP and LTD. D1 shows 150 discrete conductance states showing enhancement and inhibition modulations with significant linearity. The NL values obtained from the formulated fits are 0.07, 0.16, respectively. the closer the NL value is to zero, the better the linearity of the curves, indicating that our device exhibits good linearity in LTP/LTD. D2 also shows up to 124 discrete conductance states with NL values of 0.15 and 0.27, respectively. D0 also shows up to 120 discrete conductance states with NL values of 0.11 and 0.23, respectively. For D0, the accuracy was 90.4% for small image recognition, and the accuracy of recognizing large images is close to 86.7%

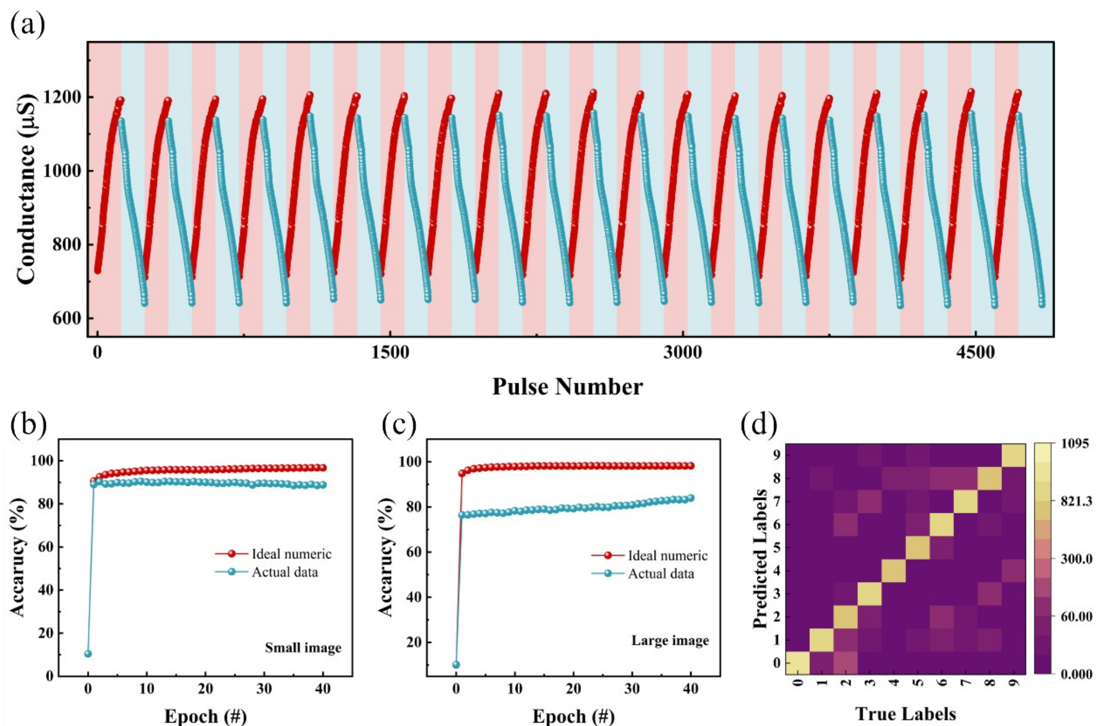

Fig. S10 D2 of (a) 20-times LTP and LTD loops, (b) training accuracies for the small image test dataset and (c) the large image test dataset. (d) confusion matrix.

The PD curves characterizing the device after a repetitive pulse sequence for 20 measurements are presented in Fig. S10(a). The neural network training based on this BTO device achieves high recognition accuracy (Fig. S10(b) and 10(c)). After 40 training sessions, the accuracy was 89.2% for small image recognition. And the accuracy of recognizing large images is close to 84.3%. This high recognition accuracy is based on the high linearity, symmetry and reproducibility of the synaptic device. The confusion matrix obtained by the artificial neural network after 40 rounds of training is shown in Fig. S10(d).

Table. S1. Comparison of the comprehensive performance (Ion, Energy, ON/OFF ratio and Accuracy) with memristors.

Structure	Ion	Energy	ON/OFF ratio	Accuracy	Reference
Au/TiO_2/Ti	Proton	25 MeV	3×10^3	-	8
Au/SCO/LSMO	He^+	5 keV	~ 169	-	9
Pt/STO/NSTO	Au	1 MeV	~ 2×10^3	94 %	10
Ti/$LiNbO_3$/Ti	Ar^+	100 eV	~ 10	-	11
Au/$LiNbO_3$/Pt/SiO_2/$LiNbO_3$	Ar^+	100 eV	~ 10^4	-	12
Pt/TiO_x/p^{+2}-Si	Ar^+	5 keV	140	-	13
Pt/BTO/$NSTO_3$	Xe^{31+}	516 MeV	~ 10^5	92.5 %	This work

References

1 W. P. Cheng, C. H. Li, C. Zhou, Y. D. He, R. H. Wei, L. Hu, W. H. Song, X. B. Zhu and Y. P. Sun, *Thin Solid Films*, 2022, **762**, 7.
2 J. Kim, A. I. Inamdar, Y. Jo, H. Woo, S. Cho, S. M. Pawar, H. Kim and H. Im, *Acs Appl. Mater. Interfaces*, 2016, **8**, 9499-9505.
3 O. Kapur, D. K. Guo, J. Reynolds, Y. S. Han, R. Beanland, L. D. Jiang, C. H. de Groot and R. M. Huang, *Adv. Electron. Mater.*, 2022, **8**, 9.
4 E. Mikheev, B. D. Hoskins, D. B. Strukov and S. Stemmer, *Nat. Commun.,* 2015, **6**, 1.
5 S. J. Dong, H. Liu, Y. Wang, J. Bian and J. Su, *Acs Appl. Mater. Interfaces*, 2024, **16**, 19235-19246.
6 J. X. Zhang, H. F. Li, T. Liu, S. J. Dong, S. Xu, H. L. Li and J. Su, *J. Appl. Phys.*, 2023, **133**, 10.
7 Y. Wang, J. Su, G. Ouyang, S. Geng, M. Ren, W. Pan, J. Bian and M. Cao, *Adv. Funct. Mater.,* 2024, **34**.
8 H. J. Song, Y. D. Liu, J. Q. Yan, X. L. Zhong, J. B. Wang and H. X. Guo, *Appl. Phys. Lett.*, 2023, **122**, 7.
9 X. Xiang, J. Rao, Z. He, M. Zhou, Q. Huang, Y. Gao, Z. Fan, X. Wang and Y. Chen, . *Appl. Phys.*, 2022, **132**.
10 H.-L. Li, J. Su, M.-H. Xu, S.-J. Dong, J. Bian, P.-S. Shan, R.-W. Wang, Y. Liu, X.-L. Wang, S.-Q. Fan, M.-H. Cao, T. Liu, T. Xu, W.-J. Kong and T. Liu, *Appl. Phys. Lett.*, 2024, **124**.
11 Q. Xie, X. Pan, W. Luo, Y. Shuai, H. Zeng, J. Wang, Y. Liu, X. Yang, L. Lv, J. Xu, H. Yan, C. Wu and W. Zhang, *Nanoscale*, 2023, **15**, 14257-14265.
12 Q. Xie, X. Q. Pan, W. B. Luo, Y. Shuai, C. G. Wu, J. J. Wang, S. T. Huang, W. Luo and W. L. Zhang, *J. Mater. Sci. Mater. Electron.*, 2021, **32**, 20817-20826.
13 D. Hasina, M. Kumar, R. Singh, S. A. Mollick, A. Mitra, S. K. Srivastava, M. A. Luong and T. Som, *ACS Appl. Electron. Mater.*, 2021, **3**, 3804-3814.